The Aeronautical Journal (2024), **128**, pp. 2261–2280
doi:10.1017/aer.2024.38

RESEARCH ARTICLE

Artificial neural network for preliminary design and optimisation of civil aero-engine nacelles

F. Tejero[1], D. MacManus[1], A. Heidebrecht[1] and C. Sheaf[2]

[1]Centre for Propulsion Engineering, School of Aerospace, Transport and Manufacturing, Cranfield University, Bedfordshire, UK
[2]Rolls-Royce PLC., Derby, UK
Corresponding author: F. Tejero; Email: f.tejero@cranfield.ac.uk

Received: 19 December 2023; **Revised:** 24 March 2024; **Accepted:** 26 March 2024

Keywords: aero-engine; nacelle; UHBPR; ANN; machine learning

Abstract

Within the context of preliminary aerodynamic design with low order models, the methods have to meet requirements for rapid evaluations, accuracy and sometimes large design space bounds. This can be further compounded by the need to use geometric and aerodynamic degrees of freedom to build generalised models with enough flexibility across the design space. For transonic applications, this can be challenging due to the non-linearity of these flow regimes. This paper presents a nacelle design method with an artificial neural network (ANN) for preliminary aerodynamic design. The ANN uses six intuitive nacelle geometric design variables and the two key aerodynamic properties of Mach number and massflow capture ratio. The method was initially validated with an independent dataset in which the prediction error for the nacelle drag was 2.9% across the bounds of the metamodel. The ANN was also used for multi-point, multi-objective optimisation studies. Relative to computationally expensive CFD-based optimisations, it is demonstrated that the surrogate-based approach with ANN identifies similar nacelle shapes and drag changes across a design space that covers conventional and future civil aero-engine nacelles. The proposed method is an enabling and fast approach for preliminary nacelle design studies.

Nomenclature

Roman symbol

b_k	bias factor
b_p	bernstein polynomials
C	class function
C_D	nacelle drag coefficient
c	curve length
f_{max}	non-dimensional axial location of nacelle's crest
L_{nac}	nacelle length
M	mach number
M_{DR}	drag rise mach number
M_{is}	isentropic mach number
n	order of the Bernstein polynomials
r_{hi}	nacelle highlight radius
r_{if}	initial radius of curvature
r_{max}	nacelle maximum radius
r_{te}	nacelle trailing edge radius
u_k	input to the neuron
v_k	sum of the weighted inputs to the neuron (u_k) and a bias factor (b_k)
y_k	output of the neuron

Greek symbol

β_{nac}	nacelle boat-tail angle
ϵ	relative error
ϕ	activation function
ψ	normalised axial coordinate
σ	relative root mean square error
ξ	normalised radial coordinate

Acronyms

ANN	artificial neural network
CFD	computational fluid dynamics
DoF	degree of freedom
DSE	design space exploration
EoC	end-of-cruise
ESDU	engineering sciences data unit
iCST	intuitive class shape transformation
iM	increased Mach number
LOM	low order model
LHS	Latin hypercube sampling
MFCR	massflow capture ratio
OMOPSO	optimised multi-objective particle swarm optimisation
RSM	response surface model

1.0 Introduction

Although computing power continuously increases, the required time-scales for preliminary design are difficult to meet with complex and detailed numerical simulations [1]. At the early stages of the design of new concepts, thousands of combinations for the different degrees of freedom are usually considered. This includes understanding the limits of the feasible design space, trade-off analysis for key geometric variables, and sensitivities to different operating conditions. For this reason, low order models (LOM) are usually required to ensure a fast and tractable design approach [2]. Over the last years there have been notable advances to ensure that the methods can meet the conflicting requirements for fast evaluations, low uncertainty and large number of degrees of freedom and design space bounds.

Within the context of aerospace applications, a range of techniques have been considered to enable the design and optimisation of complex components [1, 3]. One of the most popular is the Gaussian process based on the Kriging interpolation method [4]. Significant improvements to its predictive accuracy have been recently achieved [5–7]. For example, He et al. [5] performed Kriging surrogate-based multi-objective optimisations in which an innovative infill sampling, expected angle-penalised length improvement (EAPLI), was proposed. The method was used for the optimisation of benchmark cases, e.g. ZDT2 or DTLZ2 [8], and an aerofoil at $M = 0.40$ in which the drag coefficient was minimised and the lift coefficient maximised. It was demonstrated that the approach was able to identify a more populated Pareto front with a greater hypervolume compared with a surrogate-based method without infills. One variation of the ordinary Kriging model is the gradient-enhanced Kriging which improves the predictive performance of the LOM by incorporating gradient information across the design space [6]. This strategy has been subsequently enhanced with a weighted gradient-enhanced Kriging approach [9] and successfully used for the inverse design process of a wing at transonic conditions at $M = 0.84$. Although Kriging-based methods have been extensively used for aerodynamic applications, their main drawback is that they require a significant amount of computational memory to build the LOM. This limits their potential use for complex applications in which a large number of samples are required. For this reason, neural networks are usually used for large datasets. Secco et al. [10] generated an artificial

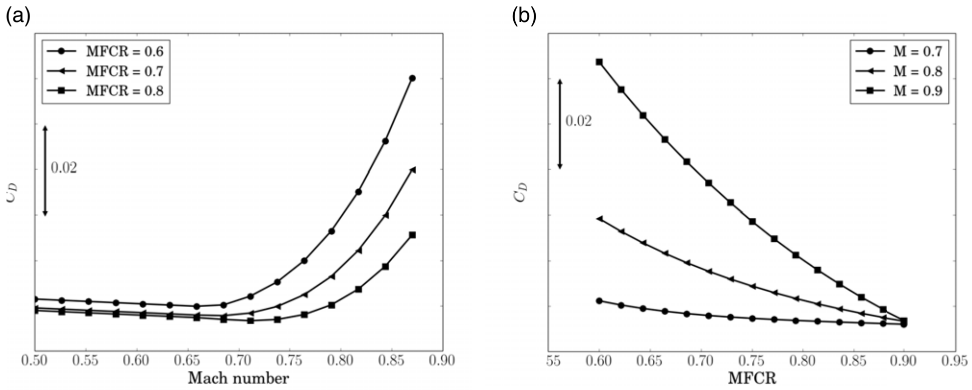

Sensitivity to Mach number

Sensitivity to massflow capture ratio

Figure 1. *Typical nacelle drag characteristics as a function of (a) Mach number and (b) massflow capture ratio.*

neural network (ANN) for the prediction of lift and drag coefficients in wing-fuselage configurations. Geometric and aerodynamic variables were used as input for the generation of the low order model, in which the aerodynamic database was generated with a full-potential code. The upper bound for the Mach number was 0.80. For an independent dataset, the generated ANN presented an absolute error of 0.0041 for the lift coefficient and of five airframe drag counts. This is a relative error lower than 5% in both metrics for an airframe at cruise conditions ($M = 0.77$). Bouhlel et al. [11] developed a scalable gradient–enhanced artificial neural network for single-point aerofoil optimisation. The LOM was generated with geometric and aerodynamic degrees of freedom, in which the maximum value of flight Mach number was $M = 0.75$. The training dataset was compiled with a RANS computational fluid dynamics (CFD) solver coupled with the adjoint method [12] and the derivatives across the design space were used to improve the neural network accuracy. For a drag minimisation case with $M = 0.72$ at $C_L = 0.82$, the CFD-based and surrogate-based optimisations yielded a similar design.

Future civil aero-engines architectures are expected to operate with high-bypass ratios to reduce the specific thrust and to improve the overall propulsive efficiency [13]. These new designs may be accompanied by an increment in the fan diameter [14] which could result in a large drag, weight, and a significant engine/airframe integration coupling [15]. As such, it is envisaged that these new configurations will use compact nacelles [16] to realise the expected performance benefits from the new engine cycles. These new design styles also pose challenges due to the expected non-linear nacelle drag characteristics of compact configurations [17]. One of the nacelle design challenges is the requirement for an acceptable aerodynamic performance at relatively high transonic Mach numbers. This is further compounded by the need to operate at a wide range of flight conditions. Across the different scenarios of the flight envelope, the nacelle aerodynamics may have strong shock-waves, shock boundary layer interaction or diffusion driven separation [18]. The nacelle drag changes, as a function of the key aerodynamic parameters of flight Mach number and massflow capture ratio (MFCR), can be non-linear (Fig. 1). For example, at a fixed flight Mach number the nacelle drag coefficient (C_D) usually increases as MFCR reduces. This is caused by the flow acceleration around the nacelle lip. For a constant MFCR, C_D sharply increases at high M because of the compressibility effects and strong shock waves that manifest at those flight regimes (Fig. 1). The sensitivity of the nacelle drag to changes in M and MFCR is a function of its shape. As such, the generation of low order models to predict the drag characteristics for different geometric and aerodynamic degrees of freedom presents significant challenges. As a consequence, preliminary tools for this complex application are very limited.

Within the context of preliminary nacelle design tools, ESDU proposed a method for estimating the drag of axisymmetric cowls at zero incidence and subsonic free-stream Mach numbers [19]. It had a prediction error of 8% on subcritical nacelle drag and of 20% on wave drag at mid-cruise conditions. This uncertainty is likely to be within the range of the expected nacelle drag benefits of compact configurations compared with conventional ones [20]. As such, more advance techniques are required for this new design challenge. In this respect, previous studies for nacelle design with low order models have also considered Kriging interpolation approaches. The majority were focused in modelling the nacelle drag at constant operating conditions and only the nacelle shape was used as input for the LOMs [21–23]. Nonetheless, this was proven to be already complex for a Gaussian process approach due to the non-linearity of nacelle drag. Tejero et al. [21] investigated an adaptive Kriging surrogate-based optimisation for a compact axisymmetric aero-engine nacelle with a normalised length of $L_{nac}/r_{hi} = 3.0$. The degrees of freedom for the LOMs comprised four nacelle geometric parameters and independent models were generated for the different transonic operating conditions that included $M = 0.85$ and 0.87. The LOMs were used within a multi-point, multi-objective optimisation process. Relative to a computationally expensive CFD-based strategy, similar nacelle designs were found at a reduction in the CFD cost of 25%. The study was extended to a 3D non-axisymmetric configuration with 20 geometric design variables [17]. As the dimensionality of the problem increased, the surrogate-based approach identified similar nacelle shapes with a 50% reduction in the computational cost compared with the baseline CFD-based method. Fang et al. [22] proposed a hybrid optimisation strategy in which RANS CFD simulations and Kriging low order models were used to drive the nacelle design process. The method was deployed for 2D axisymmetric as well as 3D non-axisymmetric configurations at transonic conditions at $M = 0.80$. Relative to baseline nacelle architectures the process yielded new shapes with a nacelle drag reduction of 4.6% and 4.0% for the 2D and 3D cases, respectively. Heidebrecht et al. [24] investigated low order models for nacelle drag prediction with geometric and aerodynamic degrees of freedom. Due to the large bounds of the design space considered, the application of ordinary Kriging methods resulted in an inaccurate LOM that did not meet the required accuracy at a preliminary design stage. For this reason, a set of surrogate models were used to decompose the problem into independent Gaussian processes. It included the exploitation of self-similarities between the drag characteristics of different nacelle shapes and their orthogonal properties, and a range of geometric filtering and tuning nuggets to focus the models accuracy in the most relevant parts of the design space. This resulted in a final set of LOMs with an acceptable predictive drag uncertainty of 3.6% for mid-cruise conditions. Nonetheless, the developed model had some simplifications that may prevent its generalisation across all the geometric and aerodynamic design space. The mid-cruise conditions, which is a key operating point, was defined to have a drag rise Mach number (M_{DR}) margin [24]. This simplifies the mid-cruise drag modelling due to the associated large non-linearity at Mach numbers above M_{DR}. In addition, geometric filters were applied to also remove regions with high non-linearity and the model's hyperparameters were tuned to obtain a good accuracy in limited operating conditions around the cruise segment.

Low order models for preliminary design with geometric and aerodynamic degrees of freedom have been used in the past for aerofoils [11], wings [10] and nacelles [24]. However, they either were developed for relatively benign conditions [10, 11, 25] or under geometric and aerodynamic assumptions to reduce the non-linearity of the problem [24]. For the investigations [10, 11, 25] in which surrogate-based optimisation was tested, this was based on single-point conditions. As such, the process only relies on one manifold of the model during the design process. The novelty of this paper is in the development of a low order model for preliminary aero-engine nacelle design, that covers regions of the design space with flight Mach numbers above 0.85, and includes a wide range of nacelle geometries beyond the typical range. In this respect, the model is built for a design space with conventional aero-engine nacelles and compact architectures that are expected for ultra high bypass ratio powerplants. The accuracy of the method is evaluated against independent datasets for the prediction of integral values of the nacelle drag characteristics. A set of multi-point, multi-objective optimisation studies are also performed and the outcomes, e.g. drag values and optimal nacelle shapes, are compared against expensive CFD-based optimisations.

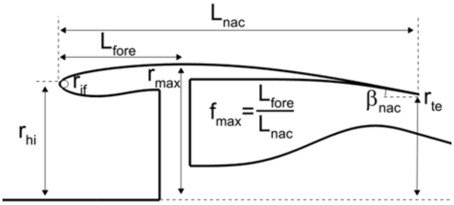

Figure 2. *Intuitive nacelle design variables.*

2.0 Methodology

The data used in this study to build low order models for 2D axisymmetric nacelles was generated with the process developed by Heidebrecht et al. [24]. It is based on a fully parametric nacelle geometry definition with a multi-block structured mesh capability, and a viscous, compressible and implicit flow solver upon which the nacelle drag is extracted from a well established thrust-drag bookkeeping method [26]. A summary of the underlying methods is provided below.

2.1 Nacelle parametrisation

The parametric definition of the nacelle geometry is controlled with an analytical approach based on the intuitive class shape transformation method (iCST) method [24]. It follows Kulfan's CST approach [27] and has been extended to use intuitive design variables. For this study, the nacelle shape is controlled with seven intuitive parameters: r_{hi}, L_{nac}, r_{te}, r_{if}, $f_{\max}$, $r_{\max}$ and β_{nac} (Fig. 2). These geometric variables may be constrained by the requirements of the intake and exhaust systems as well as integration and ground clearance considerations. For example, the nacelle trailing edge (r_{te}) is usually defined by the exhaust flow requirements and the minimum nacelle boat-tail angle (β_{nac}) is set by the external aero-line of the bypass duct. In addition, the nacelle maximum radius ($r_{\max}$) plays an important role to accommodate prescribed keep-out-zones for auxiliary components.

The general form of a CST function curve ($\xi\ (\psi)$) can be described as Equation (1):

$$\xi\ (\psi) = C_{N_2}^{N_1}\ (\psi)\ S\ (\psi) + \psi\,\Delta\xi_{te};\ \ \xi = \frac{z}{c},\quad \psi = \frac{x}{c} \tag{1}$$

where $C_{N_2}^{N_1}\ (\psi)$ is the class function, $S\ (\psi)$ is the shape function, $\Delta\xi_{te}$ defines z offset between the curve endpoints, c is the curve length in the x-direction, and x and z are the axial and radial absolute coordinates in the Cartesian space [27].

The round-nosed, sharp trailing-edge aerofoil class function is used for the parametric definition of the nacelle. This corresponds to values of $N_1 = 0.5$ and $N_2 = 1$ for the definition of the class function (Equation (2)):

$$C_{1.0}^{0.5}\ (\psi) = \psi^{0.5}\ (1-\psi) \quad \text{for} \quad 0 \le \psi \le 1 \tag{2}$$

The shape function is defined as follows (Equation (3)):

$$S\ (\psi) = \sum_{i=0}^{n} bp_i \binom{n}{i} \psi^i (1-\psi)^{n-i} \tag{3}$$

where $\binom{n}{i}$ denotes the binomial coefficients and bp_i are the different coefficients of the Bernstein polynomials.

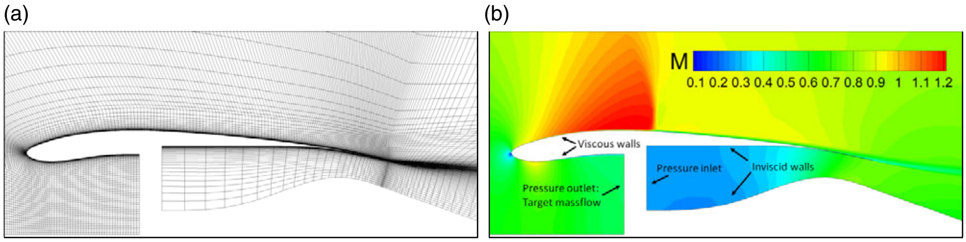

Computational grid Example of CFD solution

Figure 3. *Overview of the computational approach for nacelle applications.*

The general form for $\xi\ (\psi)$ and its first derivative can be expressed as Equations (4) and (5):

$$\xi\ (\psi) = \psi^{0.5}\ (1-\psi) \sum_{i=0}^{n} bp_i \binom{n}{i} \psi^i (1-\psi)^{n-i} + \psi\, \Delta\xi_{te} \tag{4}$$

$$\begin{aligned}\frac{\partial\xi(\psi)}{\partial\psi} &= 0.5\psi^{-0.5}\ (1-\psi) \sum_{i=0}^{n} bp_i \binom{n}{i} \psi^i (1-\psi)^{n-i} - \psi^{0.5} \sum_{i=0}^{n} bp_i \binom{n}{i} \psi^i (1-\psi)^{n-i} + \\ &+ \psi^{0.5}\ (1-\psi) \sum_{i=0}^{n} bp_i \binom{n}{i} H_{n,r}\ (\psi) + \Delta\xi_{te}\end{aligned} \tag{5}$$

where $H_{n,r}\ (\psi)$ is expressed as Equation (6):

$$H_{n,r}\ (\psi) = i\left(\psi^{i-1}\right)(1-\psi)^{n-i} - \psi^i\ (n-i)\ (1-\psi)^{n-i-1} \tag{6}$$

This mathematical derivation can be extended to any n-order derivation and obtain an analytical expression. For this specific application in which the class shape is defined with $C_{1.0}^{0.5}$, the first and last Bernstein polynomial coefficients can be analytically calculated with Equation (7):

$$bp_0 = \left(\frac{2R_{le}}{c}\right)^{0.5}\ ;\ bp_n = \tan\ (\beta) + \frac{\delta z_{te}}{c} \tag{7}$$

where R_{le} is the radius of curvature at $\psi = 0$ and $\tan\beta$ is the gradient at $\psi = 1$ [28]. For the different intuitive variables of r_{hi}, L_{nac}, r_{te}, r_{if}, $f_{\max}$, $r_{\max}$ and β_{nac}, constraints can be imposed in the form of Equations (1) and (5) to formulate a linear set of equations and obtain the coefficient of the Bernstein polynomials (bp_i). This results in a set of analytical expressions as a function of intuitive design variables.

2.2 CFD approach

The grids are automatically generated with a fully-structured multi-block domain using the commercial Ansys ICEM mesher. The first cell layer height is adjusted to have y^+ below 1. The mesh resolution is the same as reported by Heidebrecht et al. [24], and comprised approximately 40,000 cells (Fig. 3(a)). For a range of nacelle configurations at the envisaged typical cruise Mach number, it has a grid converge index [29] in the order of 1–1.5% based on a coarser and finer mesh with around 10,000 and 160,000 cells, respectively. The CFD simulations are conducted with the viscous and compressible implicit flow solver Ansys Fluent, with a double-precision and density-based approach. The primitive flow variables are obtained by resolving the Favre-averaged Navier-Stokes equations with the k-ω shear-stress transport (SST) turbulence model. A Green-Gauss node-based scheme with a second-order upwind spatial discretisation is used. The thermal conductivity is computed with the kinetic theory and the dynamic viscosity is calculated from Sutherland's law. For all simulations, the convergence criteria is based on a reduction of normalised residuals of four order of magnitude and an oscillation of the axial force on the nacelle lower than 0.05% over the last 200 iterations. The farfield is modelled with pressure-farfield conditions by imposing the Mach number, and the static temperature and pressure. The fan-face is defined with a pressure-outlet condition that uses an average static pressure, which is adjusted to fulfill a prescribed target massflow. An inlet boundary condition for the exhaust is used with farfield total pressure and temperature. This creates a generic exhaust broadly independent of specific engine design and reduces jet entrainment effects [24]. The intake and fan-cowl are specified with no-slip walls and the nozzle walls with slip conditions [24]. An example of a CFD solution obtained with the described methodology is presented in Fig. 3(b). The CFD approach has been previously validated [30], with a nacelle drag uncertainty within the cruise segment of 3.5% with respect to measurements. It is important to note that the artificial neural networks in this work cannot be validated with the available experimental data. The nacelle that was measured used a cylindrical centrebody which was typical for conventional architectures. However, the proposed nacelle parametric definition for future civil aero-engine (Section 2.1) is based on a continuous curvature distribution without a cylindrical centrebody.

2.3 Data sampling and neural network generation

The aerodynamic database was formed using six intuitive geometric variables (L_{nac}, r_{te}, r_{if}, $f_{\max}$, $r_{\max}$ and β_{nac} in Fig. 2) and covered a wide design space [24]. For example, the normalised nacelle length varied from $L_{nac}/r_{hi} = 4.5$ to 2.0, which covers conventional nacelles as well as compact civil architectures that are expected for ultra-high bypass ratio engines [31]. The aerodynamic degrees of freedom were formed by the Mach number and massflow capture, and encompassed conditions representative of the cruise-point as well as off-design [18]. The large bounds enable the building of a generalised model with enough flexibility across the design space, which is usually required at an early stage of the design process.

An adequate data sampling is a key aspect for the generation of complex low order models with non-linear data. Well-established sampling methods, such as the Latin hypercube sampling (LHS) technique [32], may not be an optimal sampling strategy for nacelle applications. Typically, it is expected that nacelle drag gradients will be greater for changes in operating conditions, especially at high Mach numbers, compared with nacelle geometry perturbations. For this reason, a mixture of approaches has been selected in which a LHS is used for the geometric space and an anisotropic sampling [33] for the aerodynamic degrees of freedom. In this respect, a greater refinement of sample points is used for high Mach numbers and low MFCRs. The Prandtl–Glauert factor ($\sqrt{1-M^2}$) [34], is used to bias the sampling density towards larger Mach numbers. For the MFCR, the sampling was selected to be linear with $\sqrt{MFCR}^{-1}$ to increase density towards lower MFCR, due to its larger nacelle drag sensitivity [31]. The upper bound for the massflow capture ratio was set to a 95% of the MFCR at which the intake would choke using an isentropic process. Conversely, the lower bound was set to MFCR = 0.5, which could be encountered at off-design conditions [18].

The ANN is built in the Python 3.7 implementation of Keras with Tensorflow as backend [35]. The ANN is composed by eight neurons as the input layer, which encompass six geometry degrees of freedom (L_{nac}, r_{te}, r_{if}, $f_{\max}$, $r_{\max}$ and β_{nac}) and two aerodynamic degrees of freedom (M and MFCR). The output layer has a single neuron that represents the nacelle drag. Both layers, i.e. input and output, are connected by a series of hidden layers. There are no general guidelines to build an ANN because it is case dependent and aspects such as the dimensionality of the problem, the number of samples or the non-linearity of the output will affect the overall neural network architecture [11]. As such, the optimal definition of hyperparameters like the number of layers, number of neurons per layer or activation function are problem-dependent. Different hyperparameters were used to fine tune the predicted accuracy of the ANNs (Table 1).

Within the context of neural network architectures, the output of each neuron (y_k) is obtained by evaluating an activation function (φ) with the sum of the weighted inputs to the neuron (u_k) and a bias factor (b_k), Equation (8):

Table 1. *Neural network hyperparameters considered*

Hyperparameter	Range
Neurons	8, 16, 32, 64, 128, 256
Hidden layers	1, 2, 3, 4, 5
Activation functions	ReLu, sigmoid, tanh

$$y_k = \varphi\left(v_k\right) = \varphi\left(u_k + b_k\right) \tag{8}$$

As part of this work, three activation functions were considered (Table 1). The rectified linear unit (ReLu) activation function (Equation (9)) is commonly used for artificial neural networks due to its simplicity [36]. The main limitation is that its gradient is equal to 0 for $v_k < 0$ [37], which can prevent learning because the neuron is not activated during the back-propagation process [38]. This activation function has been successfully demonstrated for nacelle applications in a narrow design space with modest changes in the nacelle drag response [23].

$$f_{relu}\left(v_k\right) = \max\left(0, v_k\right) \tag{9}$$

The sigmoid (Equation (10)) and hyperbolic tangent (Equation (11)) activation functions were also considered during the training process [37]. A well-known drawback of these functions is that the gradients at the bounds tends to 0 [39], which can slow down the network training because the changes in the weights and biases of the neurons are very small.

$$f_{sigmoid}\left(v_k\right) = \frac{1}{1 + e^{-v_k}} \tag{10}$$

$$f_{tah}\left(v_k\right) = \tanh\left(v_k\right) \tag{11}$$

The neural networks were trained using the Adam optimiser, a gradient descent algorithm known for its rapid convergence, computational efficiency, and scalability to large datasets [23]. A full factorial for the combination of hyperparameters presented in Table 1 was considered during the training of the different ANNs. The final selection of the artificial neural network for nacelle drag prediction was based on the minimum relative root mean square error (σ in Equation (12)) in an independent database. The validation set was generated with the same sampling strategy as the training database, i.e. LHS for the geometric variables and anisotropic for the aerodynamic ones.

$$\sigma = \sqrt{\frac{1}{N}\sum_{i=1}^{N}\epsilon^2} = \sqrt{\frac{1}{N}\sum_{i=1}^{N}\left(\frac{C_D^{CFD} - C_D^{ANN}}{C_D^{CFD}}\right)^2} \tag{12}$$

where ϵ is defined as Equation (13):

$$\epsilon = \frac{C_D^{CFD} - C_D^{ANN}}{C_D^{CFD}} \tag{13}$$

3.0 Results and analysis

Within an industrial design environment, it is required to quickly iterate through new concepts to ensure competitiveness. Surrogate models are usually used at preliminary stages of the process, where pre-trained models can enable fast design iterations. These low order models should meet the conflicting requirements of quick evaluations, sufficient accuracy and large coverage of the design space. As part of this work, the ANN architecture can make drag predictions at quasi real-time with a runtime below a fraction of second, and the database covers a wide range of architectures that include compact and conventional nacelles (Section 2.1). To assess the accuracy of the ANN model, its capabilities for nacelle drag prediction as well as for optimisation purposes have been quantified. On one hand, it is important that the integral values are accurately predicted across the geometric and aerodynamic bounds of the metamodel (Section 3.2). On the other hand, other key aspect of a response surface model (RSM) for preliminary design is to ensure that the method can successfully identify optimal nacelle configurations. In this respect, a range of multi-point, multi-objective optimisations have been performed for a range of architectures (Section 3.3).

3.1 Database generation and artificial neural network training

The ANN uses eight degrees of freedom (N_{DoF}) in which six are intuitive geometric variables ($N_{DoF-geo}$), i.e. L_{nac}, r_{te}, r_{if}, $f_{\max}$, $r_{\max}$ and β_{nac} (Fig. 2), and two are the aerodynamic variables of Mach number and massflow capture ratio. For the geometric degrees of freedom the Latin hypercube sampling method was used to sample the design space and approximately a seed of $N_{s-geo} = 600$ nacelle shapes was generated. This provides a ratio $N_{s-geo}/N_{DoF-geo} = 100$. For each nacelle configuration, an anisotropic sampling for the two operating conditions of M and MFCR was used with a total of 102 data points per configuration. Overall, this results in the generation of a database with approximately $N_s = 60{,}000$ CFD data samples, with a ratio of $N_s/N_{DoF} = 7{,}500$. Similarly, an independent dataset was generated with the same sampling techniques to quantify the ANN's accuracy in the prediction of the nacelle drag (Equation (14)). Around $N_{s-geo} = 150$ different aero-engine nacelle shapes were compiled, with a total number of approximately $N_s = 15{,}000$ CFD data points for the validation set.

$$C_D = \frac{D_{nac}}{\frac{1}{2}\rho_\infty V_\infty^2 A_{hi}} \tag{14}$$

Different flow-field topologies are encountered throughout the design space which poses many challenges in terms of the generation of accurate low order models in aero-engine nacelle applications [24]. To provide an insight of this complexity, the aerodynamic flow characteristics of two nacelle shapes compiled for the training of the neural network are showed in Fig. 4. These are presented for Mach numbers of 0.80, 0.85 and 0.90 at constant MFCR = 0.70. For Geometry 1, which has a long nacelle length with $L_{nac}/r_{hi} \approx 3.8$, there are no shocks along the cowl at $M = 0.80$ (Fig. 4(a)), and has a single shock wave at $M = 0.85$ and 0.90 with pre-shock isentropic Mach numbers of 1.19 and 1.26, respectively (Fig. 4(c) and (e)). Conversely, the short nacelle cowl with $L_{nac}/r_{hi} \approx 3.0$ of Geometry 2 has a well defined shock already at $M = 0.80$ with a pre-shock isentropic Mach number of 1.24 at the nacelle lip (Fig. 4(b)). An increase of flight velocity to $M = 0.85$ results in a change of the flow topology for which two shocks are created (Fig. 4(d)). The first one is located on the nacelle forebody with a pre-shock of 1.25 and the second is on the afterbody with a more benign intensity of pre-shock $M_{is} = 1.17$. A further increment of M to 0.90, results in the merging of both shock topoplogies in a single strong one which induces flow separation (Fig. 4(f)).

The full-factorial combination of hyperparameters summarised in Table 1 was assessed to structure independent surrogate models that can approximate the nacelle drag (Equation (14)) across the design space. The best ANN model was found with 64 neurons per hidden layer, 2 hidden layers and the ReLu activation function, with a relative root mean square error of $\sigma = 2.9\%$. This is the metamodel selected in this study for preliminary nacelle design.

3.2 Validation for nacelle drag prediction

The ANN was trained with the compiled database of 60,000 samples in Python 3.7 using the Keras library and Tensorflow as backend [35]. The training process was performed in an AMD EPYC 7543 32-core CPU with one NVIDIA A100 GPU. Once the model was trained, the surrogate can be interrogated with any workstation with the same Python environment. Testing has been successfully conducted on a conventional PC with 4GB of RAM (random access memory). As discussed above, the predictive accuracy of the ANN was evaluated with the independent dataset that was generated for perturbations

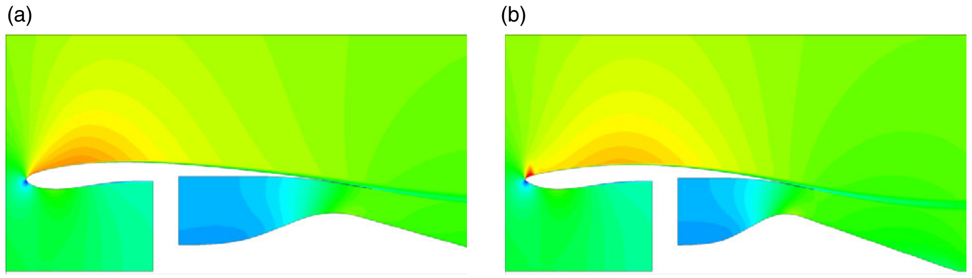

Geometry 1: M = 0.80, MFCR = 0.70 Geometry 2: M = 0.80, MFCR = 0.70

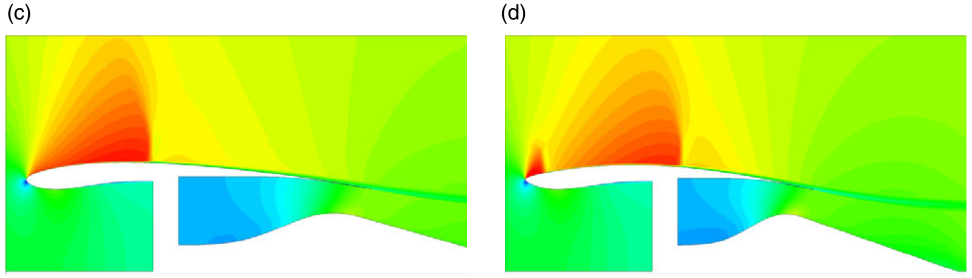

Geometry 1: M = 0.85, MFCR = 0.70 Geometry 2: M = 0.85, MFCR = 0.70

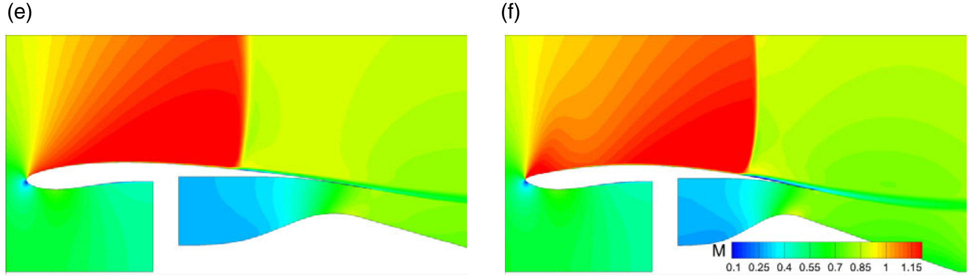

Geometry 1: M = 0.90, MFCR = 0.70 Geometry 2: M = 0.90, MFCR = 0.70

Figure 4. *Example of flow-field across the design space: Geometry 1 ($L_{nac}/r_{hi} \approx 3.8$) and Geometry 2 ($L_{nac}/r_{hi} \approx 3.0$).*

in geometric and aerodynamic degrees of freedom. Figure 5 presents the cross-validation between the ANN predictions and the CFD results across all the design space. The overall uncertainty is $\sigma = 2.9\%$, in which 92% of the cases have an error (ϵ in Equation (13)) below 5%, 7% of the evaluations present an error between 5% and 10%, and only 1% depict an error above 10%. The majority of the cases with $\epsilon > 10\%$ have a MFCR < 0.65, which is an off-design condition. The nacelle stagnation point moves closer to the fan face and this results in a large region of acceleration along the nacelle lip that may terminate with high peak Mach numbers, strong shock waves and shock induced separation [18]. For this work, an overall model uncertainty of 5% is targeted to meet the requirements of low order models for preliminary design [40]. As such, the predictive accuracy across the design space fulfills this target ($\sigma = 2.9\%$) and the ANN can be used at a preliminary stage of the design process.

Although nacelle design is a multi-point, multi-objective optimisation problem [31], and therefore an acceptable accuracy of the metamodel across the RSM bounds is needed (Fig. 5), the cruise condition has a notable importance in the overall design process. For this reason, the relative root mean square error (σ) was also quantified for expected mid-cruise type conditions. In this respect, two extra cross-validations were performed for flight Mach numbers of 0.80 and 0.85 at fixed MFCR = 0.70 (Fig. 6). These are representative of cruise-type conditions for medium-range and long-range applications, respectively.

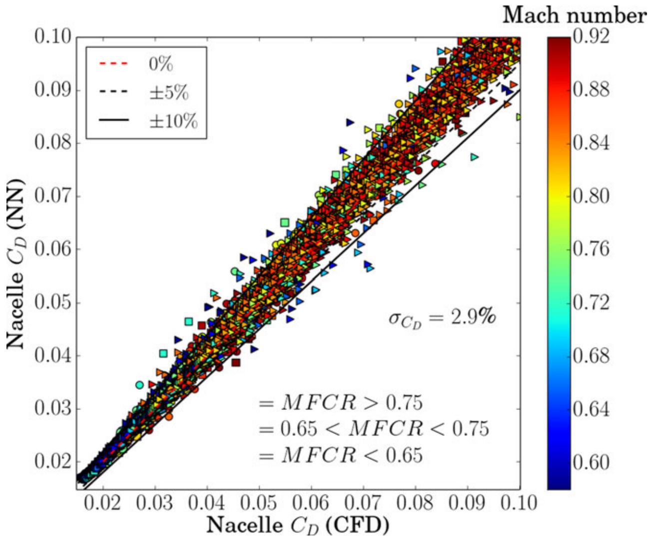

Figure 5. *ANN cross-validation of the full design space with geometric and aerodynamic degrees of freedom.*

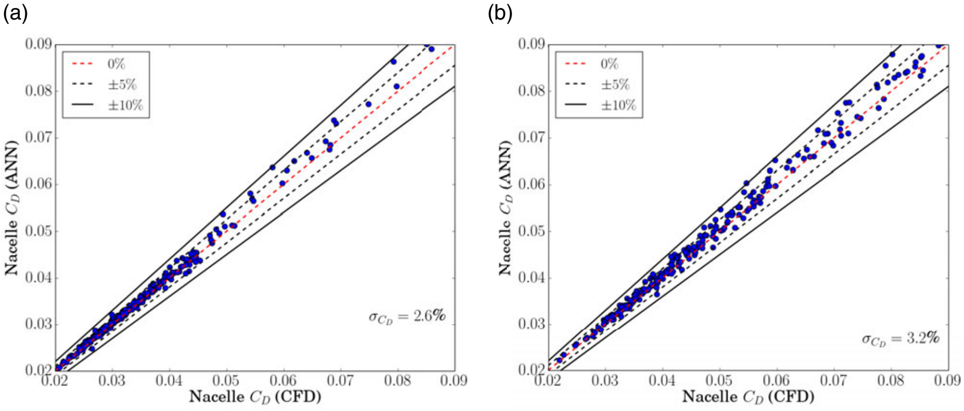

M = 0.80, MFCR = 0.70

M = 0.85, MFCR = 0.70

Figure 6. *ANN cross validation for medium- and long-range applications at mid-cruise conditions.*

As such, the predictive accuracy is quantified for changes in the geometric design space. For the medium-range applications with $M = 0.80$, the overall $\sigma = 2.6\%$ in which 95.5% of the designs have a prediction error below 5% and the remaining configurations are within $5\% < \epsilon < 10\%$. In addition, the relative root mean square error for long-range applications with $M = 0.85$ and MFCR = 0.70 is $\sigma = 3.2\%$ in which 89.2% have $\epsilon < 5\%$, 10.4% of the nacelle are within $5\% < \epsilon < 10\%$ and 0.4% have $\epsilon > 10\%$. As it could be envisaged, the relative root mean square error (σ) is larger for the high Mach number due to the increased non-linearity of this condition.

To show how the nacelle drag changes across the design space, Fig. 7 presents the drag variation as a function of the aerodynamic degrees of freedom (M and MFCR) for three different nacelle shapes from the validation dataset. They have $L_{nac}/r_{hi} \approx 3.8$, 3.0 and 2.2, and are referred to in Fig. 7 as design A, B and C, respectively. These configurations cover a wide range of the design space that is representative of conventional and compact aero-engine nacelles for medium- and long-range applications. For the

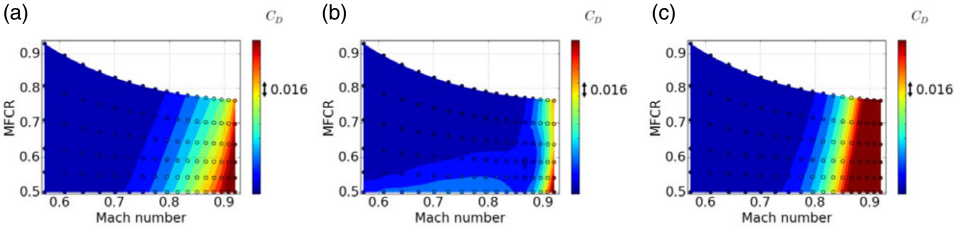

Design A: CFD Design B: CFD Design C: CFD

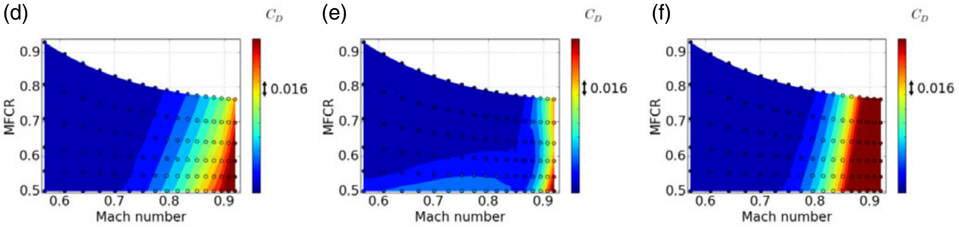

Design A: ANN Design B: ANN Design C: ANN

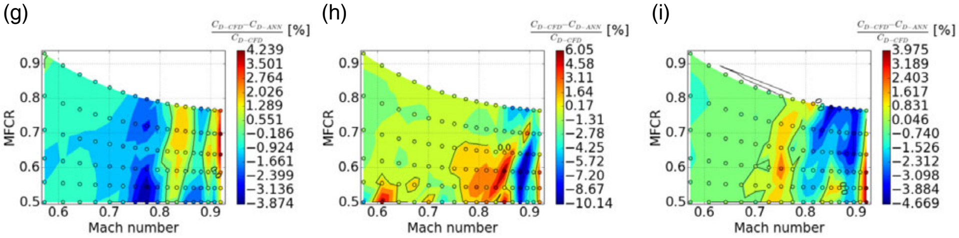

Design A: Difference Design B: Difference Design C: Difference

Figure 7. *Nacelle drag as a function of Mach number and massflow capture ratio for 3 nacelle samples: Design A ($L_{nac}/r_{hi} \approx 3.8$), Design B ($L_{nac}/r_{hi} \approx 3.0$) and Design C ($L_{nac}/r_{hi} \approx 2.2$).*

configuration with $L_{nac}/r_{hi} \approx 3.8$ (design A) the changes in nacelle drag as a function of Mach number and massflow capture ratio are benign. For a fixed MFCR, C_D smoothly increases as a function of flight Mach number caused by compressibility effects and shock-waves that are formed on the nacelle (Figs. 7(a) and (d)). Similarly, at a constant M the nacelle drag coefficient increases when MFCR is reduced due to the larger flow acceleration around the nacelle lip caused by the movement of the stagnation point towards the fan. For this nacelle configuration the ANN successfully predicts the drag changes across the wide aerodynamic design space within $0.55 < M < 0.925$ and $0.5 < \text{MFCR} < 0.93$ with a maximum absolute error of $\epsilon = 4.2\%$ (Fig. 7(g)). For the nacelle design with $L_{nac}/r_{hi} \approx 3.0$ (configuration B) the influence on C_D of M and MFCR is different relative to A. For the design B the sensitivity to a change of MFCR is modest and the changes on C_D are mainly dominated by Mach number (Fig. 7(b) and (e)). For a MFCR below 0.65, the drag rise curve has a local minima caused by the changes on the shock topology. For benign values of M, the nacelle aerodynamics are governed by a single shock. An increment in Mach number results in the change of the flow-field topology to a double shock structure with relatively low values of pre-shock M_{is}. This effect reduces the nacelle drag due to a reduction in the wave drag. Increasing further the freestream Mach number results in the combination of both shocks into a single strong one that has associated high levels of wave drag [31] and a concomitant larger nacelle drag. Modelling this non-linearity with a generalised low order model that contains configurations with such characteristics (e.g. design B) as well as designs with benign changes on C_D (e.g. design A) is complex. For this reason, previous Kriging methods filtered and smoothed non-monotonic drag-rise behaviours to enable the generation of a RSM with an acceptable predictive accuracy [24]. However, the proposed ANN is able to include the described nacelle drag characteristics without simplifications in the drag response of the nacelle. For the design B, the maximum absolute predictive error across the aerodynamic DoF is $\epsilon = 10\%$ at $M \approx 0.86$ and MFCR ≈ 0.6 (Fig. 7(h)). Lastly, the configuration C with $L_{nac}/r_{hi} \approx 2.2$ has a notable sensitivity to flight Mach number (Figs. 7(c) and (f)). This is caused by the high curvature distribution along the fancowl of this short nacelle which induces a strong flow acceleration. For this reason, the drag sensitivity to Mach number is greater than for designs A and B. For example, for flight Mach numbers above 0.85, the design C is operating post drag rise across the different MFCR which poses many challenges for a RSM due to the associated large drag gradients. Despite its complexity, the ANN predicts the changes on C_D as a function of M and MFCR with a maximum absolute error of 4.7% (Fig. 7(i)).

Within the context of preliminary nacelle design, it is important to note that the normalised nacelle length (L_{nac}/r_{hi}) is a key geometric variable because it has the biggest influence on surface area and, thus, nacelle drag and mass. Although the target may be to shorten the nacelle as much as possible, the lower bound is usually determined by the intake and exhaust length requirements [41, 42]. Trade-off studies on this variable are needed to ensure that low values of L_{nac}/r_{hi} do not result in nacelle drag penalties caused by shock losses that arise due to fancowls with high curvature and large flow accelerations [31]. In addition, the non-dimensional nacelle trailing edge (r_{te}/r_{hi}) is constrained by the exhaust shape and its flow requirements. The lower bound of the nacelle boat-tail angle (β_{nac}) is imposed by the outer bypass duct requirements and the normalised maximum radius ($r_{\max}/r_{hi}$) is usually bounded by the compromise between installed ground clearance considerations and the requirement of keep-out-zones for auxiliary components outside of the fan case, e.g. thrust reverser unit. For the purpose of providing an insight of how the neural network may be deployed in the preliminary design phase, the normalised geometric variables L_{nac}/r_{hi}, r_{te}/r_{hi}, β_{nac} and $r_{\max}/r_{hi}$ are fixed, and the two remaining ones, i.e. $f_{\max}$ and $r_{if}/_{hi}$, vary to quantify their influence on the nacelle drag characteristics. Figure 8 presents the effect of $f_{\max}$ and r_{if}/r_{hi} on C_D for two different configurations with lengths of $L_{nac}/r_{hi} \approx 3.8$ (Figs. 8(a) and (c)) and $L_{nac}/r_{hi} \approx 3.0$ (Figs. 8(b) and (d)). This is shown for representative mid-cruise conditions of long-range applications with $M = 0.85$ and MFCR $= 0.70$. The maps with the ANN are compared with higher-fidelity CFD data, where it is highlighted the good agreement in nacelle drag between the numerical simulations and the ANN predictions. Across the range of $f_{\max}$-r_{if}/r_{hi}, there is a maximum error of 2.2% and 3.0% for the configuration with $L_{nac}/r_{hi} \approx 3.8$ and $L_{nac}/r_{hi} \approx 3.0$, respectively. This deviation is within an overall $\sigma = 3.2\%$ of the model for mid-cruise conditions (Fig. 6(b)). Across the $f_{\max}$-r_{if}/r_{hi} space, the nacelle drag changes by approximately 96% for the short design ($L_{nac}/r_{hi} \approx 3.0$) and by 30% for the long configuration ($L_{nac}/r_{hi} \approx 3.8$). This greater sensitivity of the compact nacelle is expected to be due to the higher non-linearity of this region of the design space [31]. The location of the minimum C_D as a function of $f_{\max}$ and r_{if}/r_{hi} changes with the nacelle style (Fig. 8) and is well predicted by the ANN, which establishes confidence in the low order model for the design of aero-engine nacelles.

3.3 Validation for optimisation studies

Although it is important to ensure that a low order model has a sufficient predictive accuracy (Section 3.2), another key aspect is that the gradients of the performance metrics across the design space are well predicted. This is to ensure that key decisions in terms of the feasibility of new concepts are correct. Furthermore, it is fundamental that the geometric design variables of optimal configurations are appropriately identified to ensure confidence in their imposition as constraints in the design and optimisation of other sub-systems. For this reason, it is required to test the capability of response surface models in optimisation environments. In this respect, a set of surrogate-based optimisations were carried out with the neural network model and compared with the equivalent computationally expensive CFD-based ones [17, 31]. As previously described, two of the nacelle design variables (L_{nac}/r_{hi} and r_{te}/r_{hi}) are usually fixed by the intake and exhaust housing components. For this reason a range of independent multi-point, multi-objective optimisations within the range of $2.7 < L_{nac}/r_{hi} < 3.6$ and $0.90 < r_{te}/r_{hi} < 1.0$ were performed. During this process, the other variables, i.e. r_{if}/r_{hi},$f_{\max}$, $r_{\max}/r_{hi}$ and β_{nac} (Fig. 2),

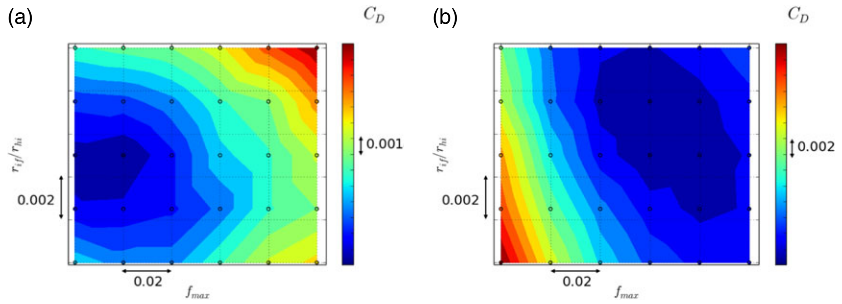

$L_{nac}/r_{hi} \approx 3.8$: CFD $L_{nac}/r_{hi} \approx 3.0$: CFD

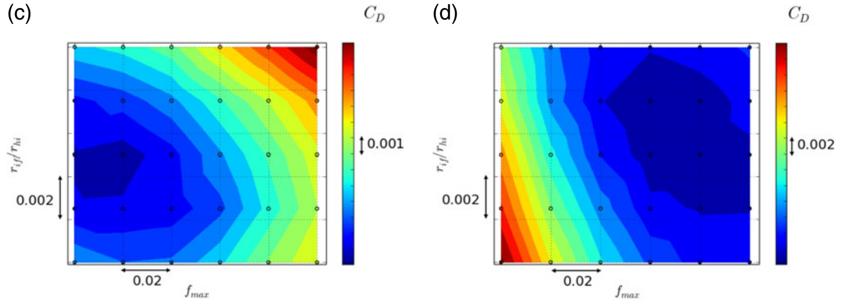

$L_{nac}/r_{hi} \approx 3.8$: ANN $L_{nac}/r_{hi} \approx 3.0$: ANN

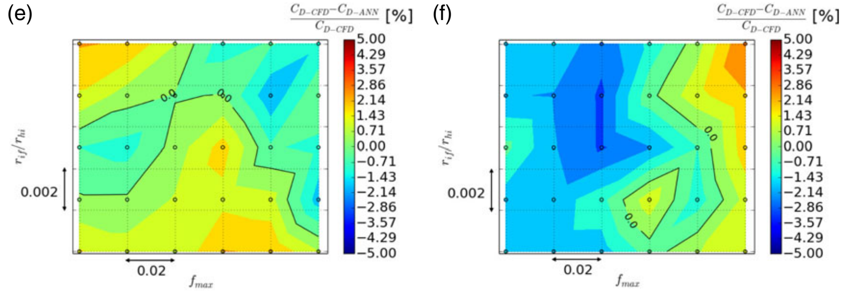

$L_{nac}/r_{hi} \approx 3.8$: Difference $L_{nac}/r_{hi} \approx 3.0$: Difference

Figure 8. *Nacelle drag as a function of the intuitive design variables $f_{\max}$ and r_{if} for two nacelle samples with $L_{nac}/r_{hi} \approx 3.8$ and 3.0.*

varied. The optimisations were performed with a well-established approach [31], in which three different conditions that are encountered in the cruise segment were evaluated. They are mid-cruise as well as the sensitivity to Mach number and mass flow capture ratio (Table 2). This analysis was carried out for long-range applications because it is the most challenging scenario for a low order model in civil aero-engine nacelle applications.

The optimisation process for both ANN-based and CFD-based approaches is coupled with the OMOPSO algorithm [43]. The selection of this gradient-free method is based on its suitability for aero-engine nacelle applications [44]. The process starts with a design space exploration (DSE) based on a LHS sampling to efficiently cover the design space. It is formed by 400 different designs to provide a ratio between the DSE size and degrees of freedom of 100. Subsequent generations of the OMOPSO process are followed by 50 nacelle designs. The optimisation convergence is monitored by means of the hypervolume indicator. The optimisation is stopped when the hypervolume changes below 1.0% in three consecutive generations.

To demonstrate the capability of the nacelle design approach, CFD-based and ANN-based optimisations are initially performed for a compact aero-engine with $L_{nac}/r_{hi} = 3.0$ and r_{te}/r_{hi}=1.0. For the same configuration, a previous RSM-based optimisation with a Gaussian regression method based on

Table 2. *Flight conditions considered during the multi-point, multi-objective nacelle optimisation process*

Condition	Mach no.	MFCR
Cruise	0.85	0.70
increased Mach number (iM)	0.87	0.70
End-of-cruise (EoC)	0.85	0.65

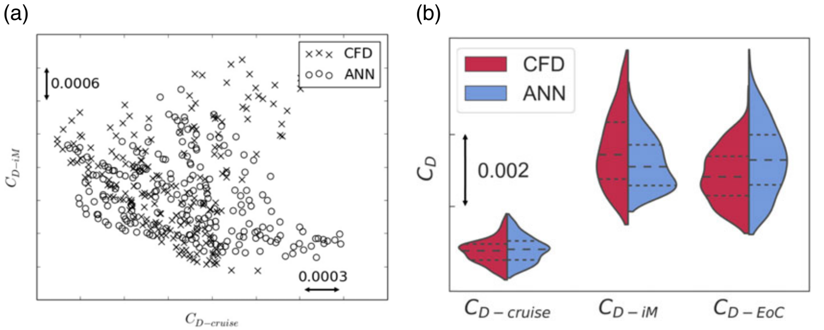

Set of optimal solutions: Pareto front

Box plot for Pareto front (Objectives functions)

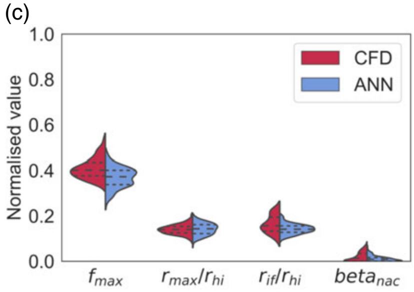

Box plot for Pareto front (Design variables)

Figure 9. *Comparison for the ANN- and CFD-based multi-point, multi-objective optimisations.*

Kriging highlighted the challenges of identifying the same optimal design space as a computationally expensive CFD in-the-loop approach [21]. This was caused by the non-linearity of the nacelle drag characteristics of this compact architecture and the difficulties associated with Kriging modelling. After successful convergence of the multi-point, multi-objective optimisation with the ANN surrogate-based and the CFD-based strategies, a set of Pareto optimal solutions were identified (Fig. 9(a)). The 3D surface is projected in the $C_{D-cruise}$-C_{D-iM} space, where the trade-off between the two objective function can be observed. The comparison of the Pareto surface for both optimisation strategies reveals the capability of the ANN-based to identify a similar shape. The hypervolume of the computationally expensive CFD in-the-loop is only 2.6% larger than the RSM-based one. Relative to the CFD in-the-loop, the minimum drag $C_{D-cruise}$ identified by the ANN is 0.2% greater. This changed to 1.0% for the minimum achievable C_{D-iM} and a reduction of 0.2% for C_{D-EoC} (Fig. 9(b)). These differences are within the predictive uncertainty $\sigma = 2.9\%$ of the ANN model (Fig. (5)). The greatest discrepancy is identified for the increased Mach number case (Table 2) with $M = 0.87$ due to the expected greater uncertainty of the ANN as the freestream Mach number increases. Another key aspect of a surrogate-based multi-point, multi-objective optimisation is to ensure that it converges to the same regions of the design space. For all the design variables ($f_{\max}$, $r_{\max}/r_{hi}$, r_{if}/r_{hi} and β_{nac}), the normalised mean values of the Pareto

Table 3. *Multi-point, multi-objective optimisation for aero-engine nacelles*

	Variable	Description
Minimise	$C_{D-cruise}$	Nacelle drag at mid-cruise conditions
by varying	f_{max}	Non-dimensional axial location of the nacelle crest
	r_{max}/r_{hi}	Non-dimensional nacelle maximum radius
	r_{if}/r_{hi}	Non-dimensional initial forebody radius
	β_{nac}	Boat-tail angle
Subject to	$C_{D-iM} < K_1 \cdot C_{D-cruise}$	Threshold for nacelle drag sensitivity at increased Mach number
	$C_{D-EoC} < K_2 \cdot C_{D-cruise}$	Threshold for nacelle drag sensitivity to reduced MFCR

front are similar between the CFD-based and RSM-based multi-point, multi-objectives optimisations (Fig. 9(c)). The maximum normalised difference is of 0.04 for $f_{\max}$, which reduces to 0.001, 0.02 and 0.008 for $r_{\max}/r_{hi}$, r_{if}/r_{hi} and β_{nac}, respectively. As such, it can be concluded that the neural network is able to drive the optimisation process to similar regions of the design space relative to the computationally expensive CFD in-the-loop approach. This establishes confidence for its deployment for optimisation purposes. It is important to note that previous studies based on CFD-based optimisations with gradient-free methods concluded that the convergence of the multi-point, multi-objective optimisation required the evaluation of approximately 1,850 designs. These were composed by 400 nacelles in the design space exploration (DSE) followed by 29 generations of 50 individuals each [45]. The same settings were used in this work for the CFD-based optimisation, which results in a total of 5,550 independent CFD evaluations, i.e. 1,850 designs with three flight conditions per design. This is usually not acceptable within a preliminary design stage due to the large overhead in terms of computing requirements and overall time to perform the optimisation.

Having established confidence that the developed approach identifies similar designs as the computationally expensive CFD-based approach, the method was used for a wide range of nacelle configurations with different L_{nac}/r_{hi} and r_{te}/r_{hi}. In this respect, a full factorial combination for values of $L_{nac}/r_{hi} = 2.7$, 3.0, 3.3 and 3.6, and $r_{te}/r_{hi} = 0.90$, 0.95, 1.0 were considered. This is to quantify if the surrogate-based approach can predict the nacelle drag gradients across the design space as well as to identify the associated geometric design variables of the optimal configurations. For each of the 12 nacelle configurations, an independent multi-point, multi-objective optimisation (Table 2) was carried out in which the process was driven with ANN predictions and CFD simulations. For all the optimisations, the process resulted in a set of Pareto optimal solutions upon which a nacelle was downselected (Table 3). The downselection criteria can be modified according to the parameters K_1 and K_2 (Table 3) depending on the requirements and relative importance that the designer wants to provide to the sensitivity to Mach number (C_{D-iM}) and MFCR (C_{D-EoC}). The overall process results in the generation of drag maps to quantify the nacelle drag changes across the design space for different L_{nac}/r_{hi} and r_{te}/r_{hi}. For the CFD in-the-loop optimisation, the nacelle mid-cruise drag changes by about 16% across the design space (Fig. 10). The non-dimensional nacelle length (L_{nac}/r_{hi}) has a larger impact on the drag variations than r_{te}/r_{hi}. For a fixed $r_{te}/r_{hi} = 1.0$, $C_{D-cruise}$ reduces by 13.4% when the nacelle length is shortened from $L_{nac}/r_{hi} = 3.6$ to 3.1. For a conventional configuration with $L_{nac}/r_{hi} = 3.6$, the changes in r_{te}/r_{hi} between 1.0 and 0.90 have a negligible effect on the mid-cruise nacelle drag. Conversely, for a compact aero-engine nacelle with $L_{nac}/r_{hi} = 3.0$, the nacelle drag increases by 4.0% when the trailing edge radius is moved inboards from $r_{te}/r_{hi} = 1.0$ to 0.90. For the short nacelle configuration with $L_{nac}/r_{hi} = 2.8$, there was not a design that fulfilled the downselection criteria (Table 3) for the most compact $r_{te}/r_{hi} = 0.90$. Similar mid-cruise drag changes were identified for the ANN-based optimisations with a variation of about 15% across the range of L_{nac}/r_{hi} and r_{te}/r_{hi} investigated (Fig. 10). The effect of L_{nac}/r_{hi} on nacelle drag is also comparable to the findings of the CFD in-the-loop optimisations. For the RSM-based cases, the mid-cruise nacelle drag decreased by 13% when the nacelle length reduced from $L_{nac}/r_{hi} = 3.6$ to 3.1 at fixed $r_{te}/r_{hi} = 1.0$. This is close to the findings from the computationally expensive CFD studies that showcased a reduction

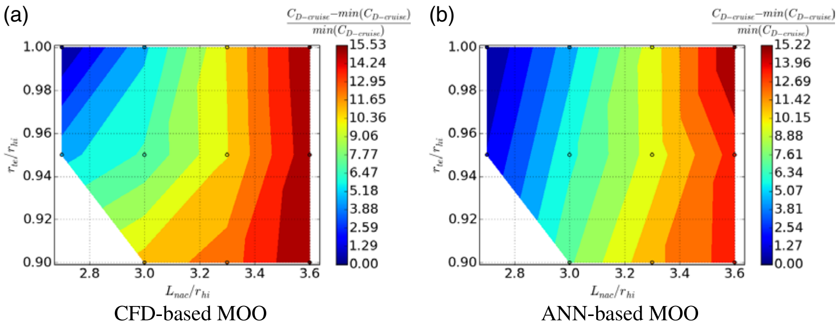

CFD-based MOO

ANN-based MOO

Figure 10. *Mid-cruise nacelle drag changes as a function of* L_{nac}/r_{hi} *and* r_{te}/r_{hi} *for downselected designs from the multi-point, multi-objective optimisations.*

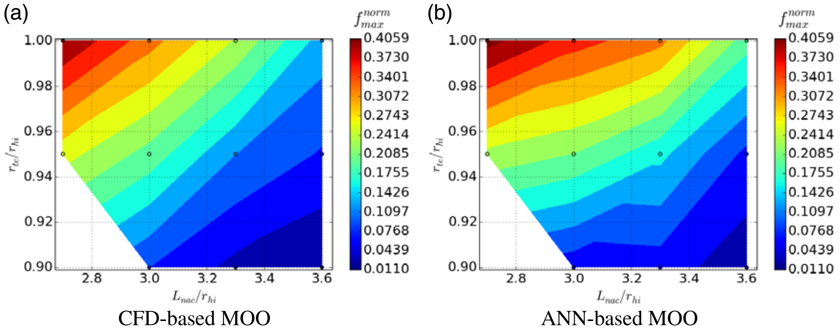

CFD-based MOO

ANN-based MOO

Figure 11. *Changes of the normalised intuitive variable* $f_{\max}$ *as a function of* L_{nac}/r_{hi} *and* r_{te}/r_{hi} *for downselected designs from the multi-point, multi-objective optimisations.*

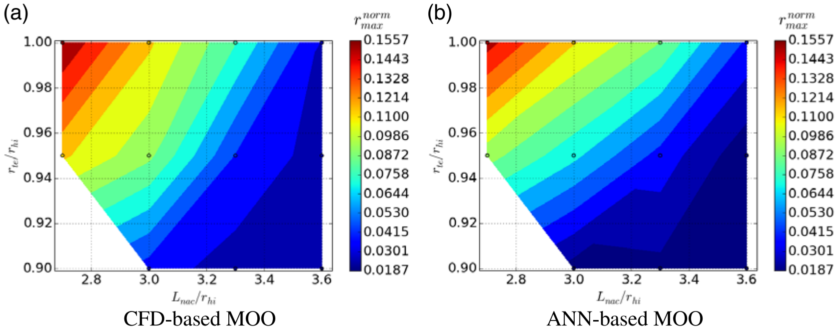

CFD-based MOO

ANN-based MOO

Figure 12. *Changes of the normalised intuitive variable* $r_{\max}/r_{hi}$ *as a function of* L_{nac}/r_{hi} *and* r_{te}/r_{hi} *for downselected designs from the multi-point, multi-objective optimisations.*

of 13.4%. Lastly, the relative importance of the effect of the nacelle trailing edge (r_{te}/r_{hi}) at constant nacelle length was also similar between the ANN and CFD optimisation approaches (Fig. 10). It is demonstrated that the low order model predicts similar changes on nacelle drag across a wide dimensional space, which builds confidence in its deployment within a preliminary nacelle design process.

Other key consideration of surrogate-based multi-point, multi-objective optimisation is that the process converges to the same parts of the design space as a computationally expensive CFD in-the-loop method. In this respect, the geometric degrees of freedom of the previous downselected designs are compared for both approaches. Figures 11 and 12 show the normalised values of $f_{\max}$ and $r_{\max}/r_{hi}$, which have a larger impact on the nacelle drag characteristics than r_{if}/r_{hi} and β_{nac} [31]. This representation is useful to quantify the changes of the intuitive nacelle design variables to derive nacelle design guidelines and design styles at a preliminary stage of the design process. The maps can also be used as constraints for the design and optimisation of other sub-systems. The design variables $f_{\max}$ and $r_{\max}/r_{hi}$ increase as the nacelle is shortened and the trailing edge radius is moved outboards. This is to reduce the nacelle curvature and the flow acceleration which has a direct impact on the overall nacelle wave drag [31]. The absolute value, as well as the gradients, across the design space for both intuitive variables are very similar between the ANN- and CFD-based optimisations. It demonstrates that the developed artificial neural network can be deployed with confidence for multi-point, multi-objective optimisation studies of aero-engines nacelles.

4.0 Conclusions

The generation of low order models for transonic flow aerodynamics with Mach numbers above 0.85 is challenging due to the associated non-linearity of these flow regimes. In this respect, previous surrogate models that included geometric and aerodynamic degrees of freedom either did not consider these conditions or included simplifications to reduce the modelling challenges. Within the context of civil aero-engine nacelle optimisation with metamodels, these assumptions are incorrect because it is needed an adequate accuracy for these operating conditions. This paper has developed a surrogate model based on artificial neural networks that uses as inputs intuitive nacelle design variables as well as the key aerodynamic parameters of Mach number and massflow capture ratio. The results show the acceptable accuracy of the developed model with a relative root mean square error of 2.9% on nacelle drag across a wide design space that considers conventional and compact nacelle shapes as well as Mach numbers up to 0.92. The ANN was used in a surrogate-based optimisation routine to carry out multi-point, multi-objective optimisation studies. It is demonstrated that the changes in nacelle drag across different nacelle configurations are well predicted relative to computationally expensive CFD in-the-loop optimisations. In addition, the changes of the intuitive nacelle design variables are also captured, which establishes confidence in the method for deriving initial guidelines at an early stage of the design process. It is shown that the method can meet the conflicting requirements for rapid evaluations, accuracy, large number of input variables and design space bounds that are needed in preliminary design work.

Data availability statement. Due to commercial confidentiality agreements the supporting data are not available.

Acknowledgment. The authors thank Rolls-Royce plc for supporting this research. Partial financial support was received from the INNOVATE UK FANFARE and the INNOVATIVE UK iFAN projects.

Competing interests. The authors declare none.

References

[1] Skinner, S.N. and Zare-Behtash, H. State-of-the-art in aerodynamic shape optimisation methods, *Appl. Soft Comput.*, 2018, **62**, pp 933–962.

[2] Gallay, S. and Laurendeau, E. reliminary-design aerodynamic model for complex configurations using lifting-line coupling algorithm, *J. Aircraft*, 2016, **53**, pp 1145–1159.

[3] Martins, J.R.R.A. Aerodynamic design optimization: Challenges and perspectives, *Comput. Fluids*, 2022, **239**, pp 105391.

[4] Bayraktar, H. and Turalioglu, F.S. A kriging-based approach for locating a sampling site in the assessment of air quality, *Stochastic Environ. Res. Risk Assess.*, 2005, **19**, pp 301–305.

[5] He, Y., Sun, J., Song, P., Wang, X. and Usmani, A.S. Preference-driven Kriging-based multiobjective optimization method with a novel multipoint infill criterion and application to airfoil shape design, *Aerospace Sci. Technol.*, 2020, **96**, 105555.

[6] Ulaganathan, S., Couckuyt, I., Dhaene, T., Degroote, J. and Laermans, E. Performance study of gradient-enhanced Kriging, *Eng. Comput.*, 2016, **32**, pp 15–34.

[7] Likeng, H., Zhenghong, G. and Dehu, Z. Research on multi-fidelity aerodynamic optimization methods, *Chin. J. Aeronaut.*, 2013, **26,** (2), pp 279–286.

[8] Deb, K., Thiele, L., Laumanns, M. and Zitzler, E. Scalable multi-objective optimization test problems, Proceedings of the 2002 Congress on Evolutionary Computation, vol. 1, 2002, pp 825–830.

[9] Han, Z.H., Zhang, Y., Song, C.X. and Zhang, K. Weighted gradient-enhanced Kriging for high-dimensional surrogate modeling and design optimization, *AIAA J.*, 2017, **55**, pp 4330–4346.

[10] Secco, N.R. and Silva de Mattos, B. Artificial neural networks to predictaerodynamic coefficients of transport airplanes, *Aircraft Eng. Aerospace Technol. Int. J.*, 2017, **89,** (2), pp 211–230.

[11] Bouhlel, M.A., He, S. and Martins, J.R.R.A. Scalable gradient-enhanced artificial neural networks for airfoil shape design in the subsonic and transonic regimes, *Struct. Multidiscip. Optim.*, 2020, **61**, pp 1363–1376.

[12] Shitrit, S. Adjoint-based aerodynamic drag minimisation with trim penalty, *Aeronaut. J.*, 2021, **126**, pp 450–474.

[13] Birch, N.T. 2020 vision: The prospects for large civil aircraft propulsion, *Aeronaut. J.*, 2000, **104,** (1038), pp 347–352.

[14] Daggett, D., Brown, S. and Kawat, R. Ultra-Efficient Engine Diameter Study. Technical Report CR-2003-212309, NASA, 2003.

[15] Raghunathan, S., Benard, E., Watterson, J.K., Cooper, R.K., Curran, R., Price, M., Yao, H., Devine, R. and Crawford, B. Key aerodynamic technologies for aircraft engine nacelles, *Aeronaut. J.*, 2006, **110**, pp 265–288.

[16] Peters, A., Spakovszky, Z.S., Lord, W.K. and Rose, B. Ultrashort nacelles for low fan pressure ratio propulsors, *J. Turbomach.*, 2015, **137,** (2).

[17] Tejero F., Christie, R., MacManus, D. and Sheaf, C. Non-axisymmetric aero-engine nacelle design by surrogate-based methods, *Aerospace Sci. Technol.*, 2021, **117,** (106890).

[18] Boscagli, L., MacManus, D., Tejero, F., Sabnis, K., Babinski, H. and Sheaf, C. Characteristics of shock-induced boundary-layer separation on nacelles under windmilling diversion conditions, *AIAA J.*, 2023.

[19] ESDU. Drag of axisymmetric cowls at zero incidence for subsonic mach numbers, Tech Rep 81024, ESDU, December 1994.

[20] Tejero, F., MacManus, D., Goulos, I. and Sheaf, C. Propulsion integration study of civil aero-engine nacelles, *Aeronaut. J.*, 2023, pp 1–15.

[21] Tejero, F., MacManus, D. and Sheaf, C. Surrogate-based aerodynamic optimisation of compact nacelle aero-engines, *Aerospace Sci. Technol.*, 2019, **93**, p 105207.

[22] Fang, X., Zhang, Y., Li, S. and Chen, H. Transonic nacelle aerodynamic optimization based on hybrid genetic algorithm, 17th AIAA/ISSMO Multidisciplinary Analysis and Optimization Conference, AIAA AVIATION Forum, AIAA Paper Number 2016-3833, 2016.

[23] Tejero, F., MacManus, D., Sanchez-Moreno, F. and Sheaf, C. neural network-based multi-point, multi-objective optimisation for transonic applications, *Aerospace Sci. Technol.*, 2023, **136**, p 108208.

[24] Heidebrecht, A. and MacManus, D. Surrogate model of complex non-linear data for preliminary nacelle design, *Aerospace Sci. Technol.*, 2019, **84**, pp 399–411.

[25] Du, X., He, P. and Martins, R.R.A. Rapid airfoil design optimization via neural networks-based parameterization and surrogate modeling, *Aerospace Sci. Technol.*, 2021, **113**, p 106701.

[26] AGARDograph AG-237. Guide to in-flight thrust measurement of turbojets and fan engines, Tech Rep, AGARD Report, 1979.

[27] Kulfan, B.M. Universal parametric geometry representation method, *J. Aircraft*, 2008, **45,** (1), pp 142–158.

[28] Christie, R., Heidebrecht, A. and MacManus, D.G. An automated approach to nacelle parameterisation using intuitive class shape transformation curves, *J. Eng. Gas Turbines Power*, 2017, **139,** (6), pp 062601–1–062601–9.

[29] Roache, P. A method for uniform reporting of grid refinement studies, *J. Fluids Eng.*, 1994, **116,** (3), pp 405–413.

[30] Robinson, M., MacManus, D. and Sheaf, C. Aspects of aero-engine nacelle drag, *Proc. Inst. Mech. Eng. Part G J. Aerospace Eng.*, 2018, **233,** (5), pp 1667–1682.

[31] Swarthout, A., MacManus, D., Tejero, F., Matesanz-Garcia, J., Boscagli, L. and Sheaf, C. A comparative assessment of multi-objective optimisation methodologies for aero-engine nacelles, 33rd Congress of the International Council of the Aeronautical Sciences (ICAS), 2022.

[32] Helton, J.C. and Davis, F.J. Latin hypercube sampling and the propagation of uncertainty in analyses of complex systems, *Eng. Syst. Safety*, 2003, **81**, pp 23–69.

[33] Zhang, Z. and Li, Y. Exploration of anisotropic design space by using unified Taylor-Cokriging method, *Appl. Math. Model.*, 2022, **110**, pp 45–60.

[34] Glauert, H. The effect of compressibility on the lift of an aerofoil, *Proc. R. Soc. A*, 1928, **118**, pp 113–119.

[35] Abadi, M., Barham, P., Chen, J., Chen, Z., Davis, A., Dean, J. et al. Tensorflow: A system for large-scale machine learning, Proceedings of the 12th USENIX Symposium on Operating Systems Design and Implementation, 2016.

[36] Goodfellow, I., Bengio, Y. and Courville, A. *Deep Learning*, The MIT Press, 2016; Illustrated edition.

[37] Lau, M.M. and Lim, K.H. Review of adaptive activation function in deep neural network, Conference on Biomedical Engineering and Sciences, 2018.

[38] Hannun, A.Y., Maas, A.L. and Ng, A.Y. Rectifier nonlinearities improve neural network acostic models, International Conference on Machine Learning, Atlanta, Georgia, USA, 2013.

[39] Haykin, S. Neural Networks: A Comprehensive Foundation, Prentice Hall PTR, 1998.

[40] Torenbeek, E. *Advanced Aircraft Desgin, Conceptual Design, Analysis and Optimization of Subsonic Civil Airplanes*, Wiley, 2013.

[41] Goulos, I., Otter, J., Stankowski, T., Macmanus, D., Grech, N. and Sheaf, C. Design optimisation of separate-jet exhausts for the next generation of civil aero-engines, *Aeronaut. J.*, 2018, **122**, pp 1586–1605.

[42] Hueso-Rebasa, J., MacManus, D., Tejero, F., Goulos, I., Sanchez-Moreno, F. and Sheaf, C. Design optimisation of non-axisymmetric exhausts for installed civil aero-engines, *Aerospace Sci. Technol.*, 2023, **142**, p 108700.

[43] Sierra, M.R. and Coello Coello, C.A. Improving PSO-based multi-objective optimization using crowding, mutation and ϵ-dominance, Evolutionary Multi-Criterion Optimization, Springer Berlin Heidelberg, 2005, pp 505–519.

[44] Sanchez-Moreno, F., MacManus, D., Tejero, F., Matesanz-Garcia, J. and Sheaf, C. Robustness of optimisation algorithms for transonic aerodynamic design, Proceedings of 9th European Conference for Aeronautics and Space Sciences, EUCASS-3AF, 2022.

[45] Robinson, M.H., MacManus, D.G., Heidebrecht, A. and Grech, N. An optimisation method for nacelle design, 55th AIAA Aerospace Sciences Meeting, AIAA SciTech Forum, Paper Number 2017-0708, 2017.

Cite this article: Tejero F., MacManus D., Heidebrecht A. and Sheaf C. (2024). Artificial neural network for preliminary design and optimisation of civil aero-engine nacelles. *The Aeronautical Journal*, **128**, 2261–2280. https://doi.org/10.1017/aer.2024.38